

<https://helda.helsinki.fi>

Experimental distinction of the molecularly induced Balmer emission contribution and its application for inferring molecular divertor density with 2D filtered camera measurements during detachment in JET L-mode plasmas

JET Contributors

2022-07-01

JET Contributors , Karhunen , J S , Holm , A , Lomanowski , B , Solokha , V , Aleiferis , S , Carvalho , P , Groth , M , Lawson , K D , Meigs , A G & Shaw , A 2022 , ' Experimental distinction of the molecularly induced Balmer emission contribution and its application for inferring molecular divertor density with 2D filtered camera measurements during detachment in JET L-mode plasmas ' , Plasma Physics and Controlled Fusion , vol. 64 , no. 7 , 075001 . <https://doi.org/10.1088/1361-6587/ac6ae3>

<http://hdl.handle.net/10138/346174>

<https://doi.org/10.1088/1361-6587/ac6ae3>

cc_by

publishedVersion

Downloaded from Helda, University of Helsinki institutional repository.

This is an electronic reprint of the original article.

This reprint may differ from the original in pagination and typographic detail.

Please cite the original version.

PAPER • OPEN ACCESS

Experimental distinction of the molecularly induced Balmer emission contribution and its application for inferring molecular divertor density with 2D filtered camera measurements during detachment in JET L-mode plasmas

To cite this article: J Karhunen *et al* 2022 *Plasma Phys. Control. Fusion* **64** 075001

View the [article online](#) for updates and enhancements.

You may also like

- [The optimal beam-loading in two-bunch nonlinear plasma wakefield accelerators](#)
Xiaoning Wang, Jie Gao, Qianqian Su et al.
- [Nonlinear functional relation covering near- and far-marginal stability in ion temperature gradient driven turbulence](#)
T Nakayama, M Nakata, M Honda et al.
- [Evolution of equilibrium particle beams in plasma under external wakefields](#)
M A Bastrukov and K V Lotov








IOP | ebooks™

Bringing together innovative digital publishing with leading authors from the global scientific community.

Start exploring the collection—download the first chapter of every title for free.

Experimental distinction of the molecularly induced Balmer emission contribution and its application for inferring molecular divertor density with 2D filtered camera measurements during detachment in JET L-mode plasmas

J Karhunen^{1,2,*} , A Holm³ , B Lomanowski⁴, V Solokha³ , S Aleiferis^{1,5}, P Carvalho^{1,6}, M Groth³ , K D Lawson¹ , A G Meigs¹, A Shaw¹ and JET Contributors⁷

¹ UKAEA, Culham Science Centre, Abingdon OX14 3DB, United Kingdom

² Department of Physics, University of Helsinki, 00014 Helsinki, Finland

³ Department of Applied Physics, Aalto University, 02150 Espoo, Finland

⁴ Oak Ridge National Laboratory, Oak Ridge, TN 37831, United States of America

⁵ Institute of Nuclear and Radiological Sciences and Technology, Energy and Safety, National Center for Scientific Research 'Demokritos', Athens 15310, Greece

⁶ Instituto de Plasmas e Fusão Nuclear, Instituto Superior Técnico, 1049-001 Lisboa, Portugal

E-mail: juuso.karhunen@ukaea.uk

Received 25 February 2022, revised 11 April 2022

Accepted for publication 27 April 2022

Published 23 May 2022



Abstract

A previously presented model for generating 2D estimates of the divertor plasma conditions at JET from deuterium Balmer line intensity ratios, obtained from tomographic reconstructions of divertor camera images, was amended to consider also the Balmer emission arising from molecular processes. Utilizing the AMJUEL and H2VIBR atomic and molecular databases of EIRENE enabled also inference of the molecular divertor density from the distinguished molecularly induced emission. Analysis of a JET L-mode density scan suggests the molecularly induced emission accounting for up to 60%–70% and 10%–20% of the Balmer D_α and D_γ intensities, respectively, at the onset of detachment, while electron-ion recombination becomes increasingly dominant with deepening detachment. Similar observations were made by post-processing EDGE2D-EIRENE simulations, which indicated significant roles of molecular D_2^+ ions and vibrational excitation of the D_2 molecules as precursors for the molecularly induced emission. The experimentally inferred molecular density at the outer strike point was found to increase monotonously with decreasing strike point temperature, reaching approximately 30%–50% of the local electron density at $n_{\text{mol,osp}} = 1\text{--}2 \times 10^{20} \text{ m}^{-3}$ at $T_{\text{e,osp}} \approx 0.7 \text{ eV}$. A further steep increase by a factor of 3–5 was observed with decrease of $T_{\text{e,osp}}$ to 0.5 eV. The observations are in qualitative and reasonable quantitative agreement with EDGE2D-EIRENE predictions of $n_{\text{mol,osp}}$ within the uncertainties of the experimental data.

⁷ See the author list of 'Overview of JET results for optimising ITER operation' by J Mailloux *et al* to be published in *Nuclear Fusion Special Issue: Overview and Summary Papers from the 28th Fusion Energy Conference (Nice, France, 10–15 May 2021)*.

* Author to whom any correspondence should be addressed.



Keywords: fusion, detachment, Balmer emission, molecules, camera tomography

(Some figures may appear in colour only in the online journal)

1. Introduction

Tomographic reconstructions of filtered divertor camera images are used in several tokamaks [1–16] for resolving visible-range divertor emission characteristics in the 2D poloidal plane. These reconstructions enable localized applications ranging from investigations of impurity erosion and migration to provision of reference data for re-producing experimental divertor plasma conditions with interpretative modelling.

Recently, different methods have been demonstrated at, e.g. ASDEX Upgrade [17], MAST Upgrade [18], JET [19, 20] and TCXV [21] for using tomographic reconstructions of the deuterium Balmer line emission for inferring estimates of divertor plasma conditions, such as electron temperature, T_e , and density, n_e , atomic deuterium density, n_{at} , ionization rate, S_{ion} , and recombination rate, S_{rec} , directly based on the emission data. These methods complement the established line-integrated spectroscopic measurements of T_e [22, 23], n_e [24–26] and $S_{ion/rec}$ [23, 27, 28], offering improved localization, as well as decreased potential for misinterpretations due to line-integration effects [19, 23] and reflections from metallic wall surfaces [6, 29].

Inference of plasma conditions from the Balmer line emission relies on atomic databases, providing a link between the emission intensity and T_e , n_e and n_{at} with collisional-radiative models [30–32]. These models, however, typically consider the Balmer emission as a purely atomic process, whereas also molecular processes in the plasma are known to result in excited deuterium atoms [33–35], consequently yielding an additional emission contribution unaccounted for by the atomic models. This molecularly induced emission component has been observed to even dominate the emission of low-excitation Balmer lines at the onset of divertor detachment [34–41], introducing a risk for potential misinterpretation of the emission data, if the molecular processes are not taken into account.

Means for addressing the molecularly induced Balmer emission in the experimental estimation of the plasma conditions in the JET divertor from camera observations by the methodology presented in [19, 20] were introduced in [41] together with a brief demonstration of utilizing the distinguished emission component for inference of the molecular divertor density. This work revisits and expands the analysis of [41], providing closer experimental inspection of the different emission components and distributions of electron, atomic and molecular densities during detachment in the low-confinement mode (L-mode) with qualitative comparisons to EDGE2D-EIRENE [42–44] modelling predictions. Moreover, the role of the vibrational excitation of the molecules in the molecularly induced Balmer emission and its interpretation is discussed.

2. Estimates of molecularly induced Balmer emission contribution and molecular density from divertor camera data

The methodology presented in [19, 20] was amended by introducing the contribution of the molecularly induced emission into the optimization model for solving estimates for T_e , n_e and n_{at} from the intensity ratios of the tomographic reconstructions of the Balmer D_α (656.1 nm), D_γ (433.9 nm) and D_ϵ (393.9 nm) line emissions. The resulting estimate for the molecularly induced emission fraction can be further used to infer the molecular divertor density within the Balmer emission regions. The amended methodology presented below has been briefly introduced and benchmarked in [41]. The principle of the method is repeated here with increased attention on the treatment of vibrationally excited D_2 molecules and the individual reactions considered in the inference of the molecular density.

2.1. Expansion of optimization model with molecularly induced emission fraction

The total intensity of a spectral line emitted in an electronic transition between two energy states with principal quantum numbers p and q can be considered as a sum of emission arising from the purely atomic processes of electron-impact excitation and electron-ion recombination, as well as the molecular processes as

$$I_{p \rightarrow q} = I_{p \rightarrow q}^{at,exc} + I_{p \rightarrow q}^{at,rec} + I_{p \rightarrow q}^{mol}, \quad (1)$$

where the emission components associated with the aforementioned processes are denoted by the superscripts of the respective terms of the equation. By applying the presentation of the collisional-radiative model of the ADAS atomic database [45] to the excitation and recombination components and considering the intensity of the molecularly induced component as fraction f_{mol} of the total intensity, equation (1) can be written as

$$I_{p \rightarrow q} = \frac{1}{4\pi} \left[\underbrace{n_{at} n_e PEC_{p \rightarrow q}^{exc}(n_e, T_e)}_{\text{atomic, excitation}} + \underbrace{n_i n_e PEC_{p \rightarrow q}^{rec}(n_e, T_e)}_{\text{atomic, recombination}} \right] + \underbrace{f_{mol} I_{p \rightarrow q}}_{\text{molecular}} \approx \frac{1}{4\pi (1 - f_{mol})} \left[n_{at} n_e PEC_{p \rightarrow q}^{exc}(n_e, T_e) + n_e^2 PEC_{p \rightarrow q}^{rec}(n_e, T_e) \right]. \quad (2)$$

The photon excitation coefficients, $PEC_{p \rightarrow q}^{exc/rec}(n_e, T_e)$, provided by the ADAS database, describe the n_e - and T_e

dependence of the purely atomic emission components. The approximation of equal ion and electron densities, $n_i \approx n_e$, has been made in equation (2), corresponding to an effective charge state close to unity, $Z_{\text{eff}} \approx 1$. Potential deviations from $Z_{\text{eff}} \approx 1$ are not believed to have a significant effect on the accuracy of the method in the plasma conditions for which it is the most suitable, as discussed in [20].

The estimates for n_e and T_e are obtained from solutions of the non-analytic optimization model

$$\begin{aligned} & (PEC_{\gamma}^{\text{exc}} PEC_{\varepsilon}^{\text{rec}} - PEC_{\gamma}^{\text{rec}} PEC_{\varepsilon}^{\text{exc}}) \frac{I_{\alpha}}{I_{\varepsilon}} \\ & + (PEC_{\alpha}^{\text{exc}} PEC_{\varepsilon}^{\text{rec}} - PEC_{\alpha}^{\text{rec}} PEC_{\varepsilon}^{\text{exc}}) \frac{I_{\gamma}}{I_{\varepsilon}} \\ & + PEC_{\alpha}^{\text{exc}} PEC_{\gamma}^{\text{rec}} - PEC_{\alpha}^{\text{rec}} PEC_{\gamma}^{\text{exc}} = 0, \end{aligned} \quad (3)$$

thoroughly described and benchmarked in [19, 20] with the implicit dependencies of the PEC s not repeated here for simplicity, using a Markov Chain Monte Carlo algorithm [46, 47]. In parallel, estimates for n_{at} and f_{mol} are obtained by simultaneously optimizing the $\frac{I_{\alpha}}{I_{\varepsilon}}$ and $\frac{I_{\gamma}}{I_{\varepsilon}}$ intensity ratios against the measured values with the help of equation (2). The inclusion of the f_{mol} variable is an amendment to the original model presented in [19, 20], in which the purely atomic ADAS representation without the molecularly induced term provided only a solution for n_{at} .

The molecularly induced contributions are considered independently for D_{α} and D_{γ} emissions by introducing new optimization variables $f_{\text{mol},\alpha}$ and $f_{\text{mol},\gamma}$ into the optimization model via equation (2), as described above. The values of $f_{\text{mol},\alpha}$ and $f_{\text{mol},\gamma}$ are allowed to range freely between 0 and 0.99 with currently no ties to predictions of any physical model. Due to the decreasing trend of the magnitude of the molecularly induced contribution with increasing electronic excitation state, as observed experimentally in [35] and by post-processing EDGE2D-EIRENE simulation results in section 3.1, the D_{ε} ($p = 7 \rightarrow q = 2$) emission is assumed to be relatively unaffected by the molecular processes in comparison to D_{α} ($p = 3 \rightarrow q = 2$) and D_{γ} ($p = 5 \rightarrow q = 2$). Consequently, introduction of an $f_{\text{mol},\varepsilon}$ variable into the optimization model was not found necessary.

As discussed in [19, 20], the estimates of T_e and n_e are constrained with the help of line-integrated spectroscopic measurements. The introduction of the additional unknown variables $f_{\text{mol},\alpha}$ and $f_{\text{mol},\gamma}$ in the optimization model is allowed by tightening of these constraints. In the benchmark studies performed in [41] using synthetically generated Balmer emission with purely atomic and molecularly induced contributions, the method was found to re-produce the molecularly induced component primarily within 25% of the reference. This suggests successful preservation of the performance of the optimization model also with the increased number of unknown variables.

It is noted that, despite being described as the molecularly induced fractions here, the $f_{\text{mol},\alpha}$ and $f_{\text{mol},\gamma}$ parameters account for all emission observed in addition to the ADAS representation of the purely atomic excitation and recombination components. This includes the potential effect of re-absorption of

the deuterium Lyman ($p \rightarrow q = 1$) emission, which has been prominently observed in detached and high-recycling conditions in JET experiments [23] and simulations for ITER [48–50] and can amplify the Balmer line emission from the standard optically thin ADAS predictions due to re-population of the low excitation states [23, 51]. The potential effects of the Lyman opacity on the analysis presented here, as well as prospects for addressing it adaptively by re-calculating the ADAS PEC s according to spectroscopically resolved Lyman emission escape factors [23] will be reported elsewhere.

2.2. Inference of molecular density

Assuming that the local values of T_e , n_e , n_{mol} and the distribution of the vibrational excitation states, ν , of the hydrogen molecules are known, the molecularly induced Balmer emission intensities arising from processes involving species H^* can be calculated as

$$\begin{aligned} I_{p \rightarrow q, \text{mol}} &= \frac{1}{4\pi} A_{p \rightarrow q} n_{\text{mol}} \times \sum_{H^*} \sum_{\nu} \\ &\times \left[f_{\nu}(T_e) \times N_{\text{H}(p)/\text{H}^*}^{\text{H}^* \rightarrow \text{H}(p)}(n_e, T_e) \right. \\ &\quad \left. \times R_{\text{H}^*/\text{H}_2}^{\text{H}_2(\nu) \rightarrow \text{H}^*}(n_e, T_e, \nu) \right] \end{aligned} \quad (4)$$

with the help of the AMJUEL [52] and H2VIBR [53] atomic and molecular databases of EIRENE. Here, $A_{p \rightarrow q}$ is the Einstein coefficient for spontaneous emission in a given transition, whose population is determined by the cascading sum terms, while $\text{H}(p)$ and $\text{H}_2(\nu)$ denote H atoms on excited state p and H_2 molecules on vibrational state ν , respectively. The terms of the equation are discussed in more detail below.

The weights of the different vibrational states are given by the fractional abundances, $f_{\nu}(T_e)$, which in this work are calculated using the collisional-radiative Python tool CRUMPET [54], which solves the linearized set of collisional-radiative equations using the H2VIBR reaction rates to resolve the vibrational distribution of the H_2 molecules based on the local T_e . The CRUMPET calculations do not consider electronic transitions, omitting thus vibrational redistribution via electronically excited states, or the effect of the velocity distribution of the H_2 molecules due to lack of corresponding vibrationally resolved reaction rates in H2VIBR. More accurate predictions of the vibrational population distributions could thus be obtained by using a more complete collisional-radiative model, such as the Yacora package [33, 55, 56], as discussed in [57].

The population of the H atoms on excitation state p , resulting from molecular processes of an arbitrary species H^* , is given by the n_e - and T_e -dependent $N_{\text{H}(p)/\text{H}^*}^{\text{H}^* \rightarrow \text{H}(p)}(n_e, T_e)$ term, which is provided by AMJUEL as a ratio between the densities of $\text{H}(p)$ and H^* . The super- and subscripts of the term thus indicate the described process and its output format. Similarly, the generation of H^* from the H_2 molecules is described by $R_{\text{H}^*/\text{H}_2}^{\text{H}_2(\nu) \rightarrow \text{H}^*}(n_e, T_e, \nu)$ as a ratio between the H^* and H_2 densities. The ν dependence is considered by scaling

Table 1. AMJUEL [52] and H2VIBR [53] reactions used for calculating the population and generation terms and the cross-sections in equations (4)–(6). The reactions of H₂ molecules with both electrons and H⁺ ions are considered in the total reaction cross-sections $\langle\sigma v\rangle^{\text{H}_2(\nu)\rightarrow\text{H}_2^+}$. For the $N_{\text{H}(\text{p})/\text{H}^*}^{\text{H}^*\rightarrow\text{H}(\text{p})}$ terms, the AMJUEL reaction IDs are given with alternative endings ‘a’ and ‘d’, corresponding to reactions resulting in H_α and H_γ emission, respectively. Note that, due to accounting of H₂⁺ ions in the reaction, the AMJUEL rate for generation of H₃⁺ ions needs to be multiplied with $R_{\text{H}_2^+/\text{H}_2}^{\text{H}_2(\nu)\rightarrow\text{H}_2^+} \frac{n_{\text{H}_2}}{n_e}$ to obtain the $\frac{n_{\text{H}_2^+}}{n_{\text{H}_2}}$ ratio.

H*	Term	Reaction	Database	Reaction ID
H ₂	$N_{\text{H}(\text{p})/\text{H}_2}^{\text{H}_2\rightarrow\text{H}(\text{p})}$	H ₂ + e → ⋯ + H(p)	AMJUEL	H.12.2.2.5a/d (H _α /H _γ)
H ₂ ⁺	$N_{\text{H}(\text{p})/\text{H}_2^+}^{\text{H}_2^+\rightarrow\text{H}(\text{p})}$	H ₂ ⁺ + e → ⋯ + H(p)	AMJUEL	H12.2.2.14a/d (H _α /H _γ)
	$R_{\text{H}_2^+/\text{H}_2}^{\text{H}_2(\nu=0)\rightarrow\text{H}_2^+}$	H ₂ (ν = 0) + H ⁺ → ⋯ + H ₂ ⁺	AMJUEL	H11.2.0b
		H ₂ (ν = 0) + e → ⋯ + H ₂ ⁺	AMJUEL	H12.2.0b
	$\langle\sigma v\rangle^{\text{H}_2(\nu=0)\rightarrow\text{H}_2^+}$	H ₂ (ν = 0) + H ⁺ → H + H ₂ ⁺	H2VIBR	H2.2.012
		H ₂ (ν = 0) + e → 2e + H ₂ ⁺	H2VIBR	H2.2.014
	⋮	⋮	⋮	⋮
	$\langle\sigma v\rangle^{\text{H}_2(\nu=14)\rightarrow\text{H}_2^+}$	H ₂ (ν = 14) + H ⁺ → H + H ₂ ⁺	H2VIBR	H2.2.1412
		H ₂ (ν = 14) + e → 2e + H ₂ ⁺	H2VIBR	H2.2.1414
H ₃ ⁺	$N_{\text{H}(\text{p})/\text{H}_3^+}^{\text{H}_3^+\rightarrow\text{H}(\text{p})}$	H ₃ ⁺ + e → ⋯ + H(p)	AMJUEL	H12.2.2.15a/d (H _α /H _γ)
	$R_{\text{H}_3^+/\text{H}_2}^{\text{H}_2(\nu)\rightarrow\text{H}_3^+}$	H ₂ (ν) + H ₂ ⁺ → H ₃ ⁺ + H	AMJUEL	H11.4.0a × $R_{\text{H}_2^+/\text{H}_2}^{\text{H}_2(\nu)\rightarrow\text{H}_2^+} \frac{n_{\text{H}_2}}{n_e}$
H [−]	$N_{\text{H}(\text{p})/\text{H}^-}^{\text{H}^-\rightarrow\text{H}(\text{p})}$	H [−] + H ⁺ → ⋯ + H(p)	AMJUEL	H12.7.2a/d (H _α /H _γ)
	$R_{\text{H}^-/\text{H}_2}^{\text{H}_2(\nu=0)\rightarrow\text{H}^-}$	H ₂ (ν = 0) + e → H [−] + H	AMJUEL	H11.7.0b
	$\langle\sigma v\rangle^{\text{H}_2(\nu=0)\rightarrow\text{H}^-}$	H ₂ (ν = 0) + e → H + H [−]	H2VIBR	H2.2.013
	⋮	⋮	⋮	⋮
	$\langle\sigma v\rangle^{\text{H}_2(\nu=14)\rightarrow\text{H}^-}$	H ₂ (ν = 14) + e → H + H [−]	H2VIBR	H2.2.1413

the solution for the vibrational ground state, ν = 0, given by AMJUEL, with the help of ν-specific (up to ν = 14) cross-sections for the investigated reaction, provided by H2VIBR, according to

$$R_{\text{H}^*/\text{H}_2}^{\text{H}_2(\nu)\rightarrow\text{H}^*} = R_{\text{H}^*/\text{H}_2}^{\text{H}_2(\nu=0)\rightarrow\text{H}^*} \frac{\langle\sigma v\rangle^{\text{H}_2(\nu)\rightarrow\text{H}^*}}{\langle\sigma v\rangle^{\text{H}_2(\nu=0)\rightarrow\text{H}^*}}. \quad (5)$$

Given the experimental estimates for the molecularly induced emission components and divertor plasma conditions, provided by the optimization model discussed in section 2.1, equation (4) can be inverted to yield the molecular divertor density:

$$n_{\text{mol}} = \frac{4\pi I_{\text{p}\rightarrow\text{q},\text{mol}}}{A_{\text{p}\rightarrow\text{q}}} \left[\sum_{\text{H}^*} \sum_{\nu} \left[f_{\nu} N_{\text{H}(\text{p})/\text{H}^*}^{\text{H}^*\rightarrow\text{H}(\text{p})} \times R_{\text{H}^*/\text{H}_2}^{\text{H}_2(\nu)\rightarrow\text{H}^*} \right] \right]^{-1}. \quad (6)$$

Unlike the estimates for $f_{\text{mol},\alpha}$ and $f_{\text{mol},\gamma}$, which are allowed to range freely in the optimization process, the ν dependences of the $R_{\text{H}^*/\text{H}_2}^{\text{H}_2(\nu)\rightarrow\text{H}^*}$ terms in equation (6) make the inferred n_{mol} subject to the assumptions made on the vibrational excitation. The assumptions are further complicated by the reaction rates of AMJUEL and H2VIBR—which are also used by CRUMPET in calculation of the vibrational distributions—existing

only for hydrogen, questioning their validity for analysing deuterium plasmas due to the differences in the vibrational behaviour of the H₂ and D₂ molecules.

The molecularly induced Balmer emission is assumed to arise from processes involving the H₂ molecules, molecular ions H₂⁺ and H₃⁺ and the negative H[−] ions [33]. The AMJUEL and H2VIBR reactions required for calculations of $N_{\text{H}(\text{p})/\text{H}^*}^{\text{H}^*\rightarrow\text{H}(\text{p})}$ and $R_{\text{H}^*/\text{H}_2}^{\text{H}_2(\nu)\rightarrow\text{H}^*}$ for these species in equations (4)–(6) are listed in table 1, while a subset of the reactions discussed in [54], consisting of H2VIBR reactions dependent only on T_e, is used for the CRUMPET calculations of f_{ν} . Earlier studies [58–60] suggest that the production of D[−] ions is expected to be insignificant in comparison to H[−] at divertor-relevant temperatures due to significantly lower cross-section for the generation of D[−] from D₂ molecules via dissociative attachment than for the corresponding reaction for H₂. Consequently, cases of including and omitting the reactions involving negative ions are considered separately in this work.

Due to the emission-based nature of the method, molecular densities can only be inferred in regions with sufficient deuterium Balmer emission. Consequently, molecules residing in cold and remote regions, such as the private flux region and the divertor far SOL, in which the Balmer emission is faint or not observed, are omitted. Further discussion on the spatial restrictions of the method can be found in [20].

3. EDGE2D-EIRENE predictions of molecularly induced Balmer emission

The individual emission contributions due to H_2 , H_2^+ , H_3^+ and H^- were investigated in comparison to the purely atomic excitation and recombination components by post-processing EDGE2D-EIRENE simulations. The simulations comprise a JET L-mode density scan across a roughly similar input parameter range as the experimental density scan discussed in sections 4 and 5, with the outer divertor ranging from high-recycling to detached conditions, and are described in detail in [20]. As emphasized in [20], the simulations are considered primarily as an indicative guideline for the behaviour of the divertor conditions during low-power L-mode detachment. Case-specific re-adjustment of the anomalous radial transport coefficients and the input power to account for changes in radial particle and heat transport and the Ohmic heating power during the density scan was not performed. Accurate quantitative re-production of the plasma conditions of the discussed experimental density scan was, thus, not expected.

While the simulated outer divertor T_e was observed in [20] to cover approximately the same range as in the experiment, EDGE2D-EIRENE was found to underestimate the divertor n_e by a factor of 3–4 and, consequently, the volumetric recombination by an order of magnitude with respect to the corresponding experimental estimates. Likely due to these shortcomings, equally deep detachment as observed in the experiment was not achieved with EDGE2D-EIRENE. Hence, comparisons between the simulations and the experimental estimates in this work are predominantly qualitative, acknowledging the potential for quantitative discrepancies arising from the aforementioned inconsistencies in divertor n_e .

3.1. Contributions of different components in H_α , H_γ and H_δ emission

The molecularly induced emission contributions were calculated from the EDGE2D-EIRENE simulation output by methods described in section 2.2 with the purely atomic excitation and recombination components provided by the ADAS representation of the atomic part in equation (2). In addition to the H_α and H_γ emission, also the H_δ ($p = 6 \rightarrow q = 2$) line was considered to demonstrate the molecularly induced contribution in high-excitation emission lines. Here, H_δ acts as a proxy for H_ϵ , which is otherwise used in the experimental analysis, due to lack of the required AMJUEL and H2VIBR data for the latter. The investigation of the different emission components was made using the plasma conditions at the outer strike point through the process of detachment with the H_2 molecules at their vibrational ground state and with the distribution of the vibrational states calculated by CRUMPET.

3.1.1. Dominance of the molecularly induced component in H_α emission. At outer strike point electron temperatures of $T_{e,osp} > 2.0$ eV, the simulations suggest the electron-impact excitation yielding the strongest component of the H_α emission in figures 1(a) and (b). With decreasing temperature, the intensity of excitation component decreases steeply, while the

electron-ion recombination component increases steadily, surpassing the intensity of the excitation component at $T_{e,osp} \approx 1.5$ eV and peaking in detached conditions at $T_{e,osp} \approx 0.6$ eV. The aforementioned purely atomic emission components are consistently several orders of magnitude more intense than those induced by the H_2 molecules directly and the H_3^+ ions.

The significance of the molecularly induced emission and the importance of considering the vibrational excitation of the H_2 molecules become evident in the investigation of the H_α emission due to the H_2^+ and H^- ions in figures 1(a) and (b). Omitting vibrational excitation in figure 1(a), the H_2^+ -induced H_α intensity remains approximately an order of magnitude below that of the atomic excitation component at $T_{e,osp} > 2.5$ eV and increases to a comparable level with the purely atomic emission at $T_{e,osp} = 1.0$ – 1.5 eV before decreasing by an order of magnitude with decreasing temperature below $T_{e,osp} \approx 1.0$ eV. The inclusion of vibrational excitation of the H_2 molecules in figure 1(b) increases the H_2^+ -driven intensity by a factor of 4–5 at $T_{e,osp} < 2.5$ eV, making it the strongest single emission component, until the atomic recombination component surpasses it in deep detachment at $T_{e,osp} < 0.7$ eV.

An even more drastic effect is observed for the H^- -induced emission whose intensity increases from insignificant levels in figure 1(a) by up to four orders of magnitude to above the purely atomic component at $T_{e,osp} < 2.0$ eV via the introduction of vibrational excitation in figure 1(b). Apart from the lowest temperatures at $T_{e,osp} < 0.7$ eV, the predicted H^- -induced emission, however, remains less intense than that due to the H_2^+ ions across the studied temperature range.

The combination of the molecularly induced emission components is observed to dominate the total H_α intensity at the onset of detachment in figures 1(g) and (h). The relative contribution peaks at $T_{e,osp} \approx 1.1$ eV, approximately coinciding with the roll-over and emerging descent of the target ion current, Φ_{ot} , when the intensity of the electron-impact excitation component has decreased due to the decreasing temperature and the electron-ion recombination component is still increasing towards its peak at lower temperatures. Below $T_{e,osp} \approx 1.0$ eV, the significance of the molecularly induced H_α emission is observed to decrease with deepening detachment due to the increase of electron-ion recombination component and the decrease of the molecularly induced components presented in figures 1(a) and (b).

As discussed above, the intensities of the H_2^+ - and H^- -driven emission components increase significantly, when the vibrational excitation of H_2 molecules is considered, which is demonstrated in figures 1(g) and (h). At the vibrational ground state in figure 1(g), the molecularly induced emission contribution exceeds the 50% fraction at $T_{e,osp} \approx 1.0$ – 1.5 eV, reaching 55% at $T_{e,osp} \approx 1.2$ eV. With the vibrational excitation considered in figure 1(h), noticeably stronger dominance is observed across a wider temperature range, starting earlier in the detachment process at $T_{e,osp} < 2.2$ eV. In the deuterium-relevant case with the H^- ions ignored, a peak molecularly induced emission fraction of 86% is reached at $T_{e,osp} \approx 1.2$ eV, followed by a decrease to approximately 20% with decreasing $T_{e,osp}$ with the increasing electron-ion recombination component becoming dominant at $T_{e,osp} < 0.7$ eV. If H^- ions are

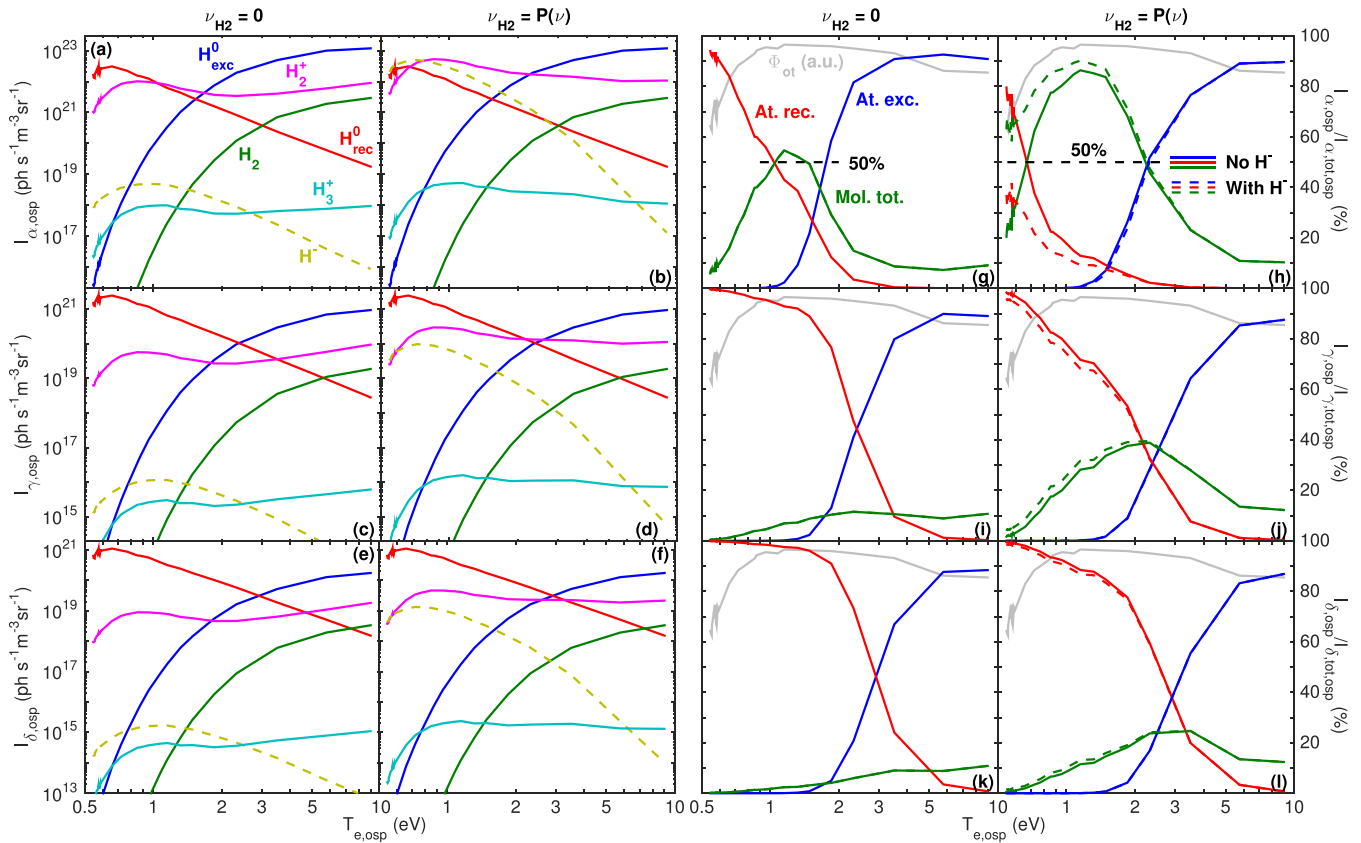


Figure 1. EDGE2D-EIRENE predictions of Balmer H_α (a), (b), H_γ (c), (d) and H_δ (e), (f) emission intensities as functions of the outer strike point electron temperature, distinguished between purely atomic electron-impact excitation (blue) and electron-ion recombination (red) and molecular processes of H_2 (green), H_2^+ (magenta), H_3^+ (cyan) and H^- (dashed yellow) with the H_2 molecules at their vibrational ground state (a), (c), (e) and with their vibrational distribution, $P(\nu)$, calculated by CRUMPET (b), (d), (f). The corresponding relative contributions of the excitation (blue), recombination (red) and total molecularly induced (green) emission components of H_α (g), (h), H_γ (i), (j) and H_δ (k), (l) with (dashed) and without (solid) inclusion of the H^- contribution with the H_2 molecules at $\nu = 0$ (g), (i), (k) and with $P(\nu)$ calculated by CRUMPET (h), (j), (l). The roll-over curve of the outer target ion current, Φ_{ot} (grey), is presented in arbitrary units in (g)–(l) as a guideline for the detachment process. The fluctuation of the curves at low $T_{e, \text{osp}}$ is due to numerical fluctuation of the simulated divertor plasma conditions at the lowest temperatures. Note the logarithmic y axes in (a)–(f) and the logarithmic x axes in all subplots.

included in the investigation, the molecular processes account for up to 90% of the total H_α emission at the roll-over point and retain the dominance also with deepening detachment, remaining above 60% even at the low end of the studied temperature range at $T_{e, \text{osp}} = 0.55$ eV.

The discussed dominating role of the H_2^+ ions in the molecularly induced and total H_α emissions is consistent with earlier modelling predictions and experimental analyses discussed in [34–36, 38–40]. Likewise, the equally significant role of H^- ions at low T_e , if negative ions are considered in the analysis, is in agreement with the comparisons presented in [34, 35].

3.1.2. Decreasing significance of molecularly induced emission with increasing electronic excitation state. The molecularly induced components of the H_γ emission in figures 1(c) and (d) and H_δ emission in figures 1(e) and (f) show similar qualitative behaviour as the corresponding H_α components in figures 1(a) and (b). However, their intensities are noticeably lower in comparison to the purely atomic

excitation and recombination components than in the case of H_α . With the vibrational excitation of H_2 considered, peak molecularly induced H_γ and H_δ emission fractions of 39% and 23%, respectively, are observed in figures 1(j) and (l), with the emission becoming increasingly more dominated by electron-ion recombination at higher excitation states. In comparison to the H_α emission, the molecularly induced H_γ and H_δ fractions were observed to peak at higher temperatures of $T_{e, \text{osp}} \approx 2.3$ – 3.5 eV and showed barely noticeable increase at lower temperatures via the inclusion of the H^- ions.

In the benchmarks performed in [41], the method discussed in section 2.1 was found incapable of distinguishing molecularly induced emission fractions below 10%. Based on the almost linear decrease of the maximum molecularly induced emission fraction as a function of the increasing principal quantum number of the electronic excitation state observed in figures 1(h), (j) and (l), the molecularly induced H_ϵ contribution—for which AMJUEL and H2VIBR do not contain the required reaction rates—is estimated to fall into the aforementioned region of uncertainty. This supports the assumption of the H_ϵ emission being relatively unaffected by

the molecular processes and the resulting simplification of not including a $f_{\text{mol},\varepsilon}$ variable in the optimization model in section 2.1.

3.2. Role of vibrational excitation in generation of H_2^+ and H^- ions

The increase in the molecularly induced Balmer emission discussed above arises from a significant increase in the generation of H_2^+ and H^- ions from H_2 molecules at vibrational excitation above the ground state. The effect was demonstrated by utilizing equation (5) and the AMJUEL and H2VIBR in table 1 to investigate individual contributions of vibrational states $\nu = 0$ –14 with their population distribution calculated by CRUMPET at different electron temperatures.

3.2.1. Population density distributions of the vibrationally excited states. The CRUMPET calculations of the vibrational distributions of the H_2 molecules in figures 2(a) and (b) suggest strong dominance of the $\nu_{\text{H}_2} = 0$ state—especially at high temperatures of $T_e > 5.0$ eV, when 80%–90% of the H_2 molecules are in their vibrational ground state. The vibrational excitation becomes more prominent with decreasing electron temperatures, and the contributions of the $\nu_{\text{H}_2} > 1$ states are observed to increase by 1–2 orders of magnitude between the $T_e = 9.0$ eV and the $T_e < 4.0$ eV cases in figure 2(a). However, even at its lowest contributions at $T_e = 1.1$ –1.9 eV, the ground state accounts for more than 53% of the H_2 molecules. The monotonous decrease of the population densities with increasing ν_{H_2} of the example distributions in figure 2(a) is confirmed as consistent behaviour at all temperatures by figure 2(b). The preference of the ground state is broadly in agreement with earlier experimental observations and modelling predictions [57, 61–67].

3.2.2. Dominance of the $\nu = 4$ state in production of H_2^+ . The low presence of the vibrationally excited states is compensated by their significantly increased production of H_2^+ ions in collisions with electrons and H^+ ions. As observed in figures 2(c) and (d), the cross-section for H_2^+ production is the highest for the $\nu_{\text{H}_2} = 4$ state consistently across the studied temperature range with the peaking becoming more emphasized at low temperatures: at $T_e = 9.0$ eV, the cross-section at $\nu_{\text{H}_2} = 4$ exceeds that at the ground state by approximately a factor of 5, while at $T_e < 2.0$ eV, the difference exceeds two orders of magnitude. The peaking is attributed to the largest overlap of the vibrational wave function of the $\nu = 4$ state of H_2 with that of the H_2^+ ions.

Even with the strong decrease of the relative population density with increasing ν_{H_2} the strong peaking of the cross-section around $\nu_{\text{H}_2} = 4$ is sufficient to cause a significant contribution in the total production of H_2^+ ions. The effective H_2^+ production cross-section in figure 2(d), obtained as a normalized sum with the help of the relative population densities in figure 2(b), can be observed to deviate from that of the ground state at $T_e < 5.0$ eV and exceed it by approximately a factor of 5 at $T_e < 2.5$ eV. When the effects of the population densities

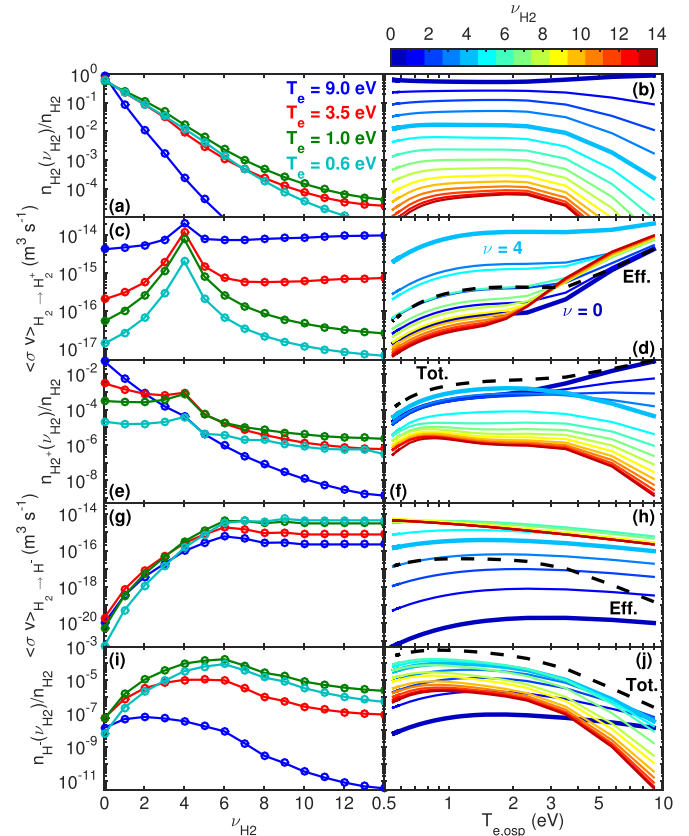


Figure 2. Relative population densities of different H_2 vibrational states (a), (b), reaction cross-sections of production (c), (d), (g), (h) and densities as fractions of the H_2 density (e), (f), (i), (j) of the H_2^+ (c)–(f) and H^- (g)–(j) ions. Subplots on the left column (a), (c), (e), (g), (i) present example distributions as functions of the vibrational state ν_{H_2} at $T_e = 0.5$ eV (cyan), $T_e = 1.0$ eV (green), $T_e = 3.5$ eV (red) and $T_e = 9.0$ eV (blue), while the right column (b), (d), (f), (h), (j) presents each ν_{H_2} state individually as functions of T_e according to the provided colour bar. In the right column, the $\nu_{\text{H}_2} = 0$ and $\nu_{\text{H}_2} = 4$ (d), (f) states have been bolded to indicate the ground state and the state with the consistently highest H_2^+ production rate. The black dashed curves represent the effective reaction cross-sections normalized with the population distributions (d), (h) or the total densities of the H_2^+ and H^- ions as fractions of the H_2 density (f), (j). Note the logarithmic y axes in all plots and the logarithmic x axis in (b), (d), (f), (h), (j).

and the cross-sections are combined, figures 2(e) and (f) suggest that more H_2^+ ions are generated from H_2 molecules at the $\nu_{\text{H}_2} = 3$ –4 states than from the ground state at $T_e < 2.5$ eV. In total, figure 2(f) indicates that the H_2^+ ions are a rare minority species in the plasma with their density ranging within 0.01%–1.0% of the H_2 density at detachment-relevant low temperatures. Nevertheless, as discussed in section 3.1, even the minor concentrations are sufficient to yield a major contribution in the Balmer H_α emission.

3.2.3. Insignificance of the vibrational ground state in production of H^- . Figures 2(g) and (h) suggest that the cross-section for the production of H^- ions from H_2 molecules at their vibrational ground state is insignificantly small in comparison to the vibrationally excited states. The cross-section

can be seen to be 30–100 times higher than at the ground state already at $\nu_{\text{H}_2} = 1$, after which it increases steeply with increasing ν_{H_2} until plateauing at $\nu_{\text{H}_2} \geq 6$ to 5–7 orders of magnitude above the cross-section at the ground state. Consequently, the effective cross-section in figure 2(h) is 2–4 orders of magnitude higher than that of the ground state with the difference increasing with decreasing T_e .

Unlike for H_2^+ ions, the cross-section for production of H^- ions is not observed to consistently peak at a distinct ν_{H_2} state. The decrease of the population densities in figures 2(a) and (b) decreases the contribution of the $\nu_{\text{H}_2} > 6$ states in the production of H^- , and figures 2(i) and (j) suggest the $\nu_{\text{H}_2} = 4$ –6 states to be the most accountable for the generation of H^- ions. Figure 2(j) indicates the total density of H^- ions to remain consistently below 0.1% of the H_2 density and to exceed the H_2^+ density only at the lowest temperatures of $T_e < 0.7$ eV.

4. Experimental estimates of molecularly induced Balmer emission during detachment in JET L-mode plasmas

The methodology discussed in section 2 was used to experimentally investigate the contribution of molecular processes in the Balmer D_α and D_γ emission in L-mode plasmas in JET. Divertor camera data was processed for pulses 94759, 94762, 94771 and 94773, comprising an L-mode density scan during which the outer divertor ranged from high-recycling conditions to deep detachment. The experiment is described in more detail in [20]. Distinction of the molecularly induced D_α and D_γ emission was briefly presented in [41] as a demonstration of the method, concentrating on the conditions at the outer strike point. The key results of [41] are repeated here in sections 4.2 and 4.3 in a wider context with additional analysis provided on the evolution and the 2D characteristics of the different deuterium emission contributions.

Previously, the closest indicator for 2D localization of the D_2 molecules in the (R, z) plane with the divertor camera system of JET has been application of a narrow bandpass filter with the central wavelength of 602.0 nm and bandwidth of 3.19 nm, which observes part of the spectral extent of the D_2 Fulcher- α band. The emission in this region is, however, strongly contaminated by continuum emission due to bremsstrahlung, which cannot be spectrally resolved from the actual Fulcher- α emission in the camera measurements. Consequently, the camera observations in the 602.0-nm region cannot be considered to provide a reliable quantitative or qualitative representation of the Fulcher- α emission. To assess the improvements in 2D characterization of the molecules in the divertor with the newly presented methods with respect to the previously available indicators, tomographic reconstructions of camera images with the 602.0-nm filter—recorded during pulse 94762, which was a similar density ramp pulse as the more thoroughly analyzed 94759—are also discussed. A purely molecular reference is provided for the analysis of the EDGE2D-EIRENE simulations by calculating the D_2 Fulcher- α intensity using the simulation output for the divertor T_e , n_e and n_{mol} and the AMJUEL H12.2.2.5f reaction data.

4.1. Spatial characteristics of the purely atomic, molecularly induced and molecular deuterium emission during detachment

The tomographic reconstructions of the Balmer D_α emission suggest concentration of the experimentally distinguished molecularly induced emission component in figures 3(g)–(i) to the vicinity of the outer strike point, while the poloidal extension of the total emission in figures 3(a)–(c) with decreasing divertor temperature is attributed to the purely atomic component in figures 3(d)–(f). At the strike point, the intensity of the molecularly induced component is observed to be comparable to the purely atomic component but showing more inclination towards the far SOL, consequently widening the spatial distribution of the total D_α emission radially near the outer strike point. Approximately similar qualitative behaviour was observed for the D_γ emission.

The spatial behaviour of the molecularly induced Balmer D_α emission deviates significantly from that of the emission around 602.0 nm in figures 3(j)–(l). While the molecularly induced Balmer emission remains in the vicinity of the outer strike point, the distribution of the emission around 602.0 nm is observed to extend and shift to above the X-point with proceeding detachment. This can partially be attributed to the potential difference between the upper and lower electronic excitation states being relatively high at approximately 14 eV for Fulcher- α , consequently pushing the emission front upstream towards higher temperatures with decreasing divertor temperature. However, especially the strong peaking above the X-point in deep detachment may also likely appear due to a strong contribution from bremsstrahlung. This is supported by camera observations during similar pulses with the W I filter at 400.96 nm, which show the emission peaking above the X-point in detached conditions, when the filter is expected to observe primarily continuum emission rather than eroded tungsten.

The expansion of the distributions of the different emission components is observed also in the poloidal profiles in figures 5(a)–(c), obtained by tracking the distributions along the path illustrated in figure 4 from the outer strike point to the X-point and vertically across it into the core plasma. Similar analysis is presented also for the corresponding emission contributions calculated from the EDGE2D-EIRENE simulation output in figures 5(d)–(f). It is noted that the EDGE2D-EIRENE prediction of the molecularly induced emission contribution is obtained using the AMJUEL and H2VIBR rates for hydrogen, as discussed earlier. For a more deuterium-relevant comparison to the experiment, the H^- ions were ignored in the calculation.

The experimentally distinguished purely atomic emission increases significantly at the outer strike point, when $T_{e,\text{osp}}$ decreases to approximately 1.0 eV due to volumetric recombination. As the temperature in the divertor volume decreases and the recombination region extends towards the X-point at $T_{e,\text{osp}} < 1.0$ eV—see [20] for poloidal investigation of T_e and S_{rec} in the divertor—the peak of the purely atomic D_α component shifts away from the strike point, and the poloidal profile becomes increasingly flat between the strike point and

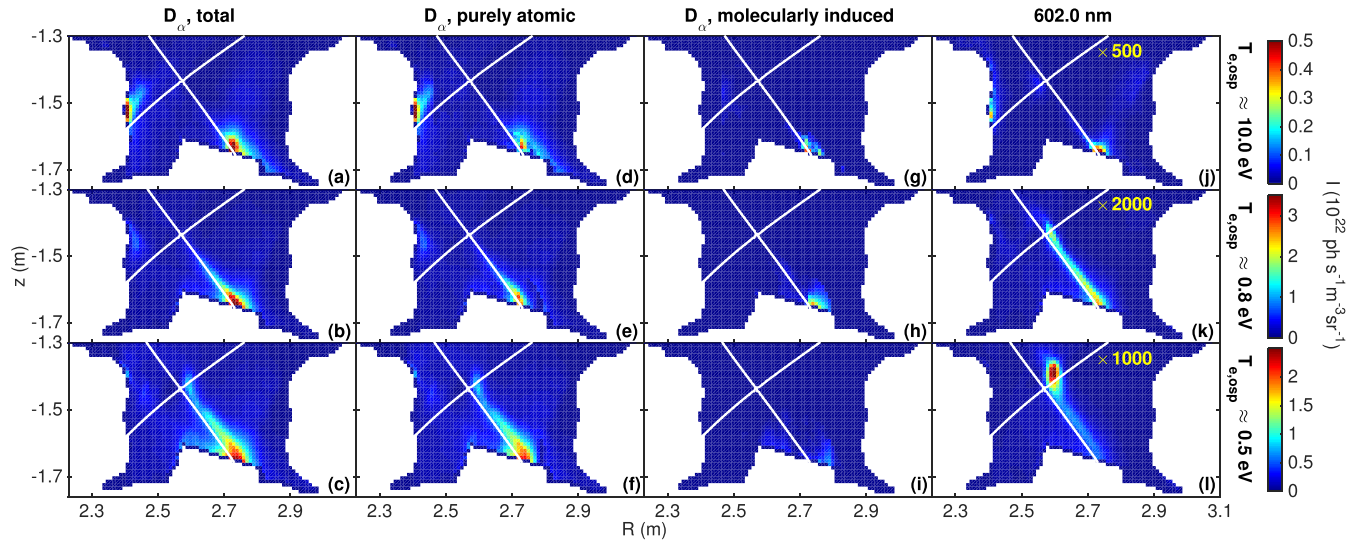


Figure 3. Tomographic reconstructions of the Balmer D_α emission (a)–(c) and its purely atomic (d)–(f) and molecularly induced (g)–(i) components, as well as the emission around 602.0 nm (j)–(l) at outer strike point electron temperatures of $T_{e,osp} \approx 10.0$ eV (a), (d), (g), (j), $T_{e,osp} \approx 0.8$ eV (b), (e), (h), (k) and $T_{e,osp} \approx 0.5$ eV (c), (f), (i), (l). The intensities in (j)–(l) have been scaled by factors of 500, 2000 and 1000, respectively, for illustrative purposes.

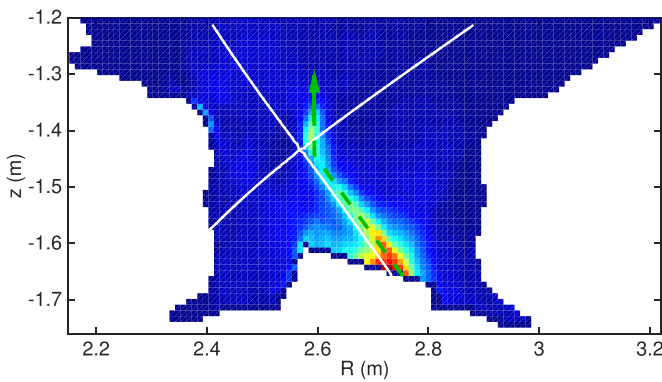


Figure 4. Path, visualized with the dashed green arrow, along which the poloidal profiles of the emission and density distributions in figures 5 and 9 are obtained.

the X-point. The EDGE2D-EIRENE predictions in figure 5(d) also show purely atomic D_α emission extending from the outer strike point to the X-point, but due to less pronounced volumetric recombination processes predicted in the simulations than in the experimental analysis, as discussed in [20], the emission profiles reflect also the movement of the ionization front upstream more prominently than in the experimental emission data.

Both the experimental analysis and the EDGE2D-EIRENE predictions show increase of the molecularly induced D_α component with decreasing $T_{e,osp}$ near the outer strike point in figures 5(b) and (e), followed by a noticeable decrease in deep detachment at the lowest temperatures. The experimental estimates in figure 5(b) suggest the molecularly induced emission remaining primarily within 5 cm from the strike point with limited extension upstream at the lowest temperatures, while flatter extension towards the X-point is predicted by the simulations in figure 5(e). As observed previously in the 2D

emission distributions in figure 3, the experimentally recorded emission around 602.0 nm in figure 5(c) shows significantly wider poloidal coverage than the molecularly induced Balmer emission with a distinct peak above the X-point at the lowest $T_{e,osp}$. In the EDGE2D-EIRENE predictions in figure 5(f), the pure Fulcher- α emission front can be seen shifting upstream, but a similar peak as in the experimental data around 602.0 nm is not observed above the X-point in deep detachment. This can partially be attributed to the simulations showing lower temperature in the X-point region than estimated experimentally in [20], being insufficient to excite as strong Fulcher- α emission. However, it is more likely an indication of the incapability of resolving the Fulcher- α emission from bremsstrahlung in the experimental camera measurements.

4.2. Evolution of purely atomic and molecularly induced D_α and D_γ contributions at the outer strike point during detachment

Local investigation of the experimentally distinguished Balmer D_α and D_γ emission components at the outer strike point in figures 6 aligns mainly with the previously presented EDGE2D-EIRENE predictions in figure 1. For clarity of visualization, the molecularly induced emission component was not divided into contributions from different molecular processes in a similar fashion as in figure 1. Based on the discussion of the EDGE2D-EIRENE predictions and the postulated lack of D^- ions, the molecularly induced emission can, however, be assumed to be primarily driven by processes involving D_2^+ ions.

Unlike the EDGE2D-EIRENE predictions in figure 1, the experimental camera observations in figures 6(a) and (c) do not show strong D_α and D_γ emission due to electron-impact excitation at $T_{e,osp} > 3.0$ eV. Instead, the D_α and D_γ intensities

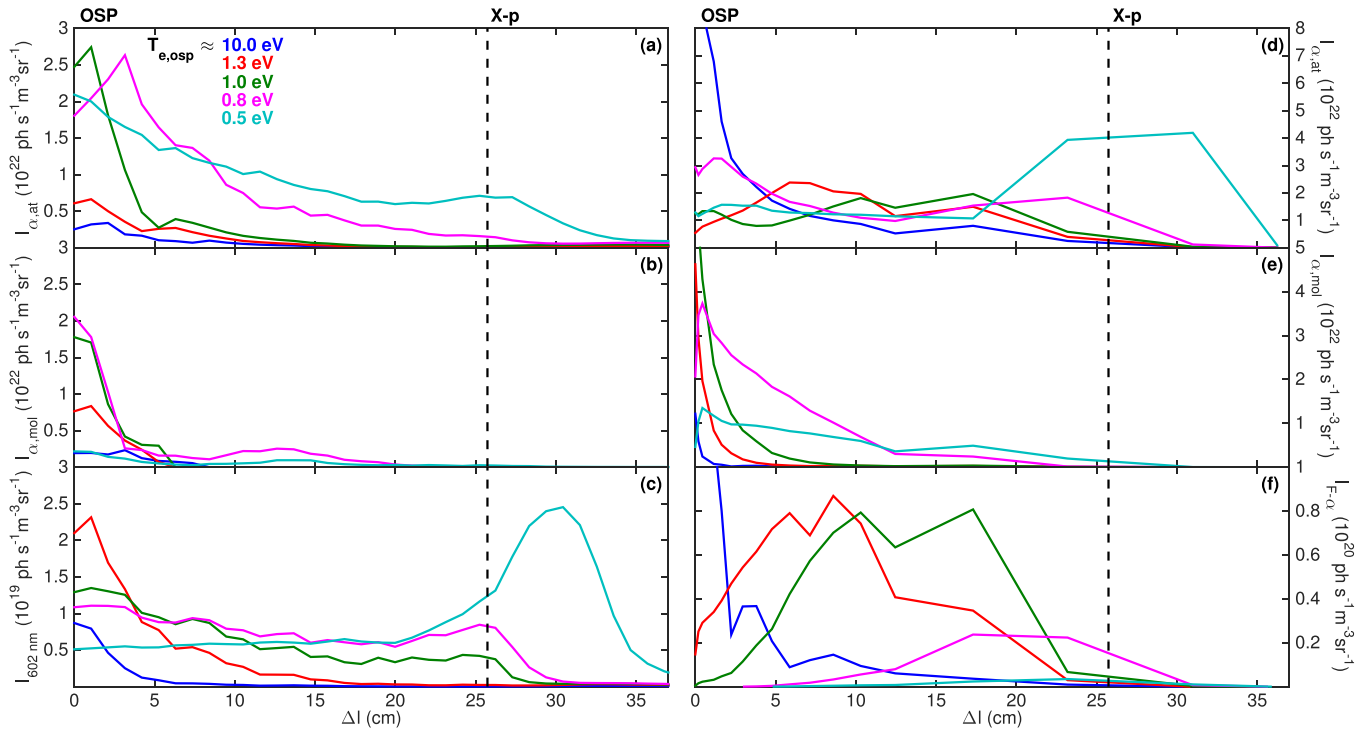


Figure 5. Experimental estimates (a)–(c) and EDGE2D-EIRENE predictions (d)–(f) of poloidal profiles of the purely atomic (a), (d) and molecularly induced (b), (e) Balmer D_α emission components, as well as the experimentally recorded emission around 602.0 nm (c) and the molecular Fulcher- α band emission derived from EDGE2D-EIRENE (f) at $T_{e,osp} \approx 10.0$ eV (blue), $T_{e,osp} \approx 1.3$ eV (red), $T_{e,osp} \approx 1.0$ eV (green), $T_{e,osp} \approx 0.8$ eV (magenta) and $T_{e,osp} \approx 0.5$ eV (cyan). The Δl coordinate measures the distance from the outer strike point ($\Delta l = 0$) along the path illustrated in figure 4. The vertical black dashed line marks the location of the X-point along the path.

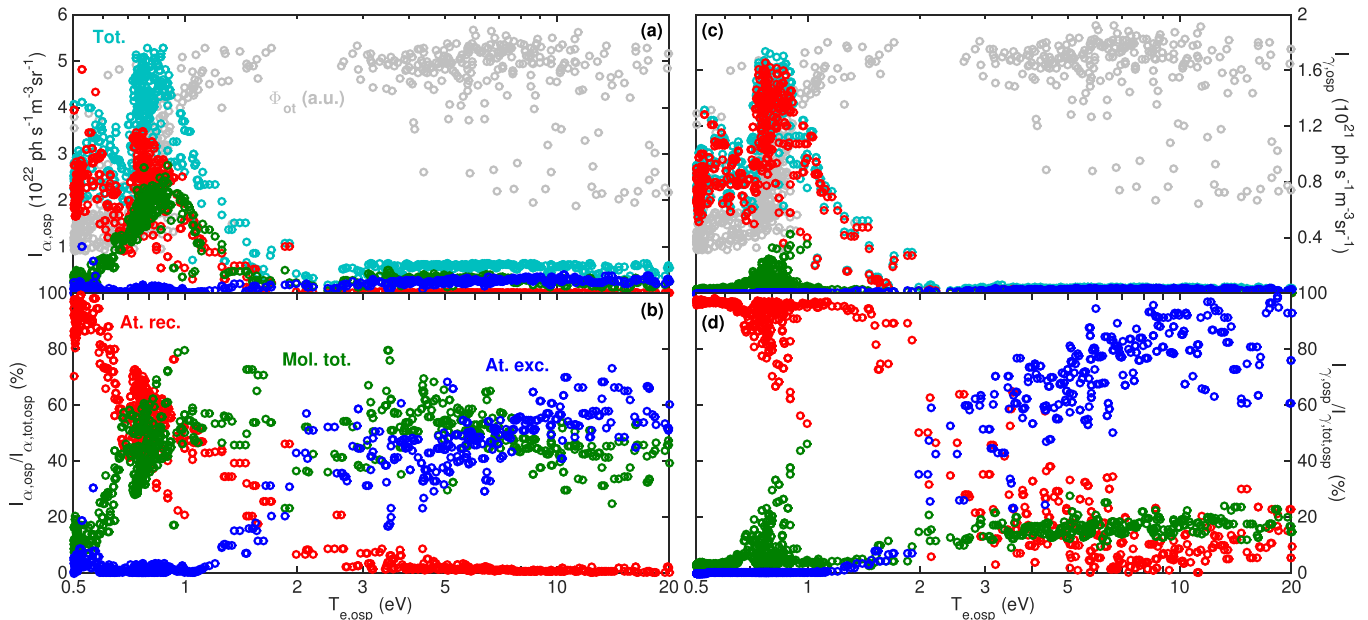


Figure 6. Total (cyan) Balmer D_α (a) and D_γ (c) emission intensities recorded at the outer strike point together with their experimentally distinguished excitation (blue), recombination (red) and molecularly induced (green) components and their respective relative fractions (b), (d) of the total intensity as functions of the outer strike point electron temperature. The outer target ion current (grey) is presented in (a), (c) in arbitrary units as a guideline for the detachment process. Note the logarithmic x axes.

remain low before increasing steeply below $T_{e,osp} < 2.0$ eV and peaking at approximately $T_{e,osp} \approx 0.8$ eV, below the roll-over temperature of $T_{e,osp}^{roll-over} \approx 1.1$ eV, defined here as the

temperature below which the plateau of the target ion current turns into a steepening descent in figures 6(a) and (c). Below $T_{e,osp} \approx 0.8$ eV, the total D_α and D_γ intensities decrease

steeply with decreasing $T_{e,osp}$ before settling at the low end of the studied temperature range.

For $T_{e,osp} > 2.0$ eV, figure 6(b) indicates approximately even division of the D_α intensity between the electron-impact excitation and molecularly induced components. It is noted that due to the low emission intensities in this temperature range, the analysis is characterized by high relative uncertainties of the order of 50%. For $T_{e,osp} < 2.0$ eV, the excitation component decreases, while the observed increase in the total emission in figure 6(a) coincides with the emergence of the electron-ion recombination component, whose contribution in the total intensity increases steadily with decreasing $T_{e,osp}$ in figure 6(b). The intensity of the molecularly induced D_α increases together with the recombination component in figure 6(a), as $T_{e,osp}$ decreases from 2.0 to 0.8 eV, with its relative contribution peaking at 60%–70% at $T_{e,osp} \approx 1.0$ eV in figure 6(b).

The maximum molecularly induced D_α emission fraction presented in figure 6(b) is somewhat lower than in the recent observations at TCv, where the molecular processes were found to account for almost 90% of the D_α emission at the onset of detachment [35, 36]. The discrepancy may partially be explained by the different wall materials between the two devices: earlier modelling interpretations of JET experiments suggest that the relative fraction of deuterium recycling from the divertor targets as D_2 molecules is approximately 30% lower with the tungsten divertor of the JET-ILW with respect to the carbon divertor of the preceding JET-C era [68, 69]. The lower molecularly induced emission fraction observed at JET may thus be a symptom of a larger share of the incoming deuterium flux being recycled as atoms instead of molecules in the tungsten divertor of JET in comparison to the carbon divertor of TCv. Moreover, the higher divertor electron densities at JET are expected to result in stronger emission component due to electron-ion recombination.

For $T_{e,osp} < 0.8$ eV, the intensity of the molecularly induced D_α component decreases with decreasing $T_{e,osp}$, and its relative contribution falls to approximately 20%, while the emission becomes increasingly more dominated by the recombination component in agreement with the EDGE2D-EIRENE predictions in figure 1. The qualitative behaviour of the total D_α intensity in figure 6(a) thus follows that of the recombination component, which is found similar to the evolution of the volumetric recombination rate at the outer strike point, presented in [20], attributed to the interplay of the simultaneous decrease in $T_{e,osp}$ and $n_{e,osp}$.

Figures 6(c) and (d) suggest significantly lower molecularly induced contributions for D_γ than presented above for D_α . The estimated molecularly induced emission fraction remains primarily within 10%–20%, approaching the limits of the method for successfully recognizing low emission contributions, as discussed in [41]. The D_γ emission is, instead, strongly dominated by the electron-ion recombination component, whose relative contribution increases rapidly to above 80% in figure 6(d) for $T_{e,osp} < 2.0$ eV, when a strong increase in the D_γ intensity is observed in figure 6(c). As for D_α , also the evolution of the D_γ emission intensity resembles

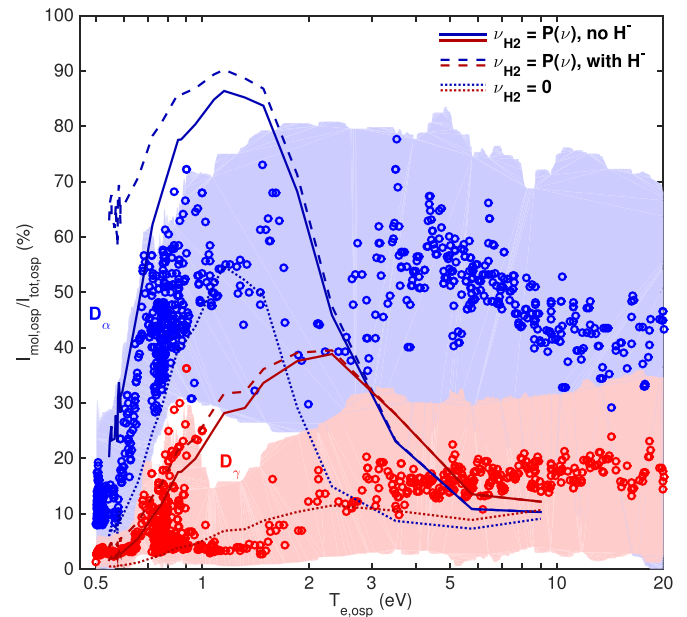


Figure 7. Experimentally estimated molecularly induced emission fractions of D_α (blue data points) and D_γ (red data points) at the outer strike point as functions of the outer strike point temperature together with EDGE2D-EIRENE predictions of the molecularly induced H_α (dark blue lines) and H_γ (dark red lines) emissions with the H_2 molecules at their vibrational ground state (dotted), as well as with their vibrational distribution calculated by CRUMPET with (dashed) and without (solid) the inclusion of H^- ions in the calculation of the emission. The shaded areas represent the error bars of the experimental estimates. Note the logarithmic x axis. Adapted from [41]. © IOP Publishing Ltd. All rights reserved.

qualitatively the behaviour of the outer strike point recombination rate presented in [20].

4.3. Indicative assessment of the validity of the assumptions made on vibrational excitation and molecular processes

A direct comparison of the experimentally estimated molecularly induced D_α and D_γ emission contributions and the EDGE2D-EIRENE predictions of the corresponding H_α and H_γ fractions in figure 7 shows qualitative and quantitative agreement between the two analyses within the uncertainties of the experimental data for $T_{e,osp} < 2.0$ eV. In this temperature range, the experimental data primarily lies within the boundaries set by the EDGE2D-EIRENE predictions with the H_2 molecules at their vibrational ground state and with the vibrational distribution provided by CRUMPET without the inclusion of the H^- ions in the calculation of the emission. For $T_{e,osp} > 2.0$ eV, the experimental data does not show a similar steep decrease in the molecularly induced emission fractions as the simulation predictions, which is attributed to the previously discussed absence of the strong electron-impact excitation component emerging in the simulations with increasing $T_{e,osp}$. With less pronounced excitation component in the simulations, a closer quantitative agreement of the molecularly induced emission fractions could be expected in figure 7 also at higher divertor temperatures.

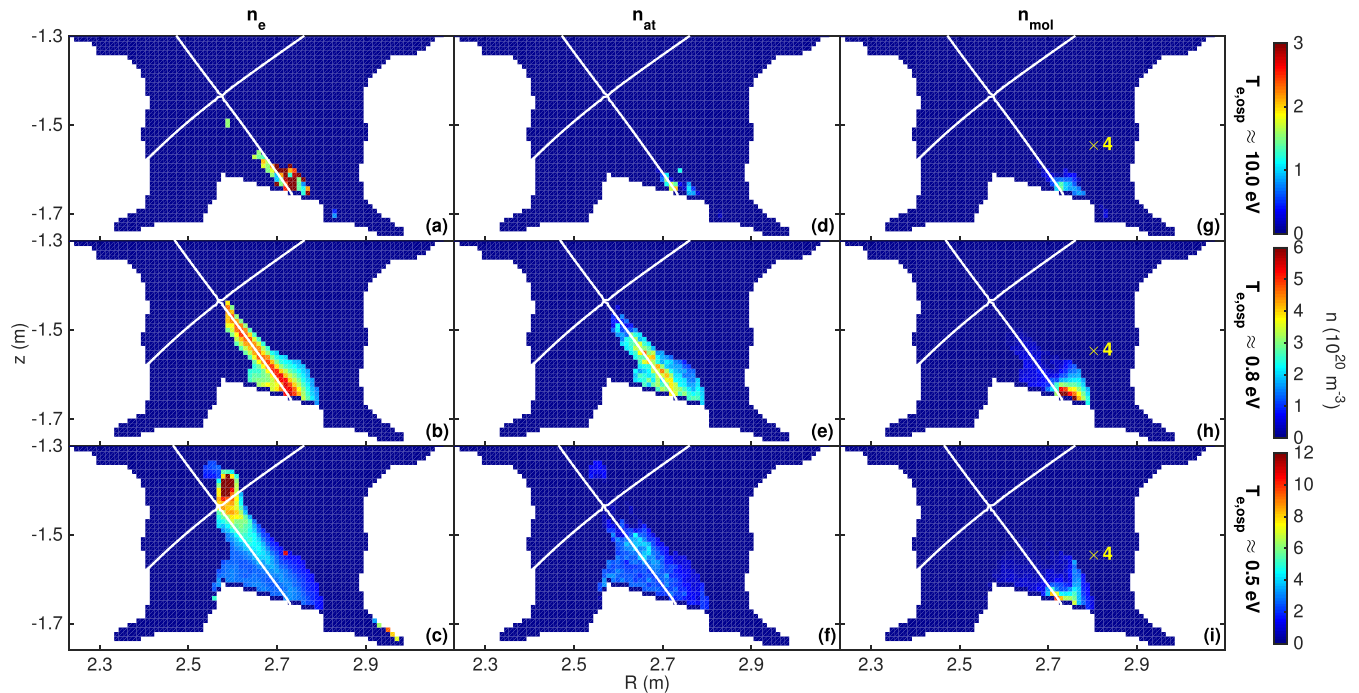


Figure 8. Experimental estimates of the 2D distributions of the electron (a)–(c), atomic (d)–(f) and molecular (g)–(i) divertor densities at outer strike point electron temperatures of $T_{e,osp} \approx 10.0$ eV (a), (d), (g), $T_{e,osp} \approx 0.8$ eV (b), (e), (h) and $T_{e,osp} \approx 0.5$ eV (c), (f), (i). The molecular densities in (g)–(i) have been scaled by a factor of 4 for illustrative purposes.

The qualitative and quantitative agreement between the solutions of the freely ranging $f_{mol,\alpha}$ and $f_{mol,\gamma}$ optimization variables in the experimental analysis and the modelling predictions based on physical models is a promising indication of the functionality of the method for successful distinction of the molecularly induced Balmer emission contribution in detached conditions. The agreement also suggests that the AMJUEL and H2VIBR reaction rates for H provide a reasonable approximation of the molecular processes also in D plasmas both in terms of calculations of the distribution of the vibrationally excited states and the molecularly induced emission. It is emphasized that an accurate re-production of the experimental data in figure 7 was not an expectation, as no attempt was made to match the divertor densities between the simulations and the experiment in [20].

If H^- ions are included in the calculation of emission from the simulation output, the molecularly induced H_α emission fraction in figure 7 remains above 60% at the low end of the studied $T_{e,osp}$ range instead of following the steep decrease observed both in the experimental data and the EDGE2D-EIRENE predictions without the consideration of H^- . This supports the previously postulated exclusion of the negative ions in analysis of D plasmas.

5. Experimental inference of molecular divertor density during detachment

The estimates of the molecularly induced Balmer D_α and D_γ emission discussed in the previous section were used to

experimentally infer the molecular divertor density within the Balmer emission regions with the methodology described in section 2.2. The analysis discussed here expands the results presented in [41] as demonstration of the method at the outer strike point—revisited here in section 5.2—to the divertor volume in 2D. The inferred molecular densities are also compared to the estimates of the electron and atomic divertor densities, obtained as solutions of the same optimization process. The introduction of the $f_{mol,\alpha}$ and $f_{mol,\gamma}$ variables in the optimization model was found to have a minimal effect on the estimated n_e due to the constraints set upon it with the help of the line-integrated spectroscopic measurements. Instead, the n_{at} estimate was found to expectedly deviate partially from the results presented in [20], as will be demonstrated in section 5.3.

5.1. Spatial distribution of molecular density

The electron density is observed to increase in a small volume within approximately 5 cm of the outer strike point with decreasing $T_{e,osp}$ before peaking at the strike point at $T_{e,osp} \approx 1.0$ eV. Further decrease in the divertor temperature is met with extension and flattening of the n_e distribution towards the X-point and ultimately a formation of a high-density peak above the X-point in deep detachment, as visualized by the 2D estimates in figure 8 and the poloidal profiles in figure 9(a), obtained in a similar fashion as in figure 5. The latter is supported by the EDGE2D-EIRENE predictions in figure 9(d). Similarly, the atomic density in figures 8(d)–(f) and 9(b) and (e) is

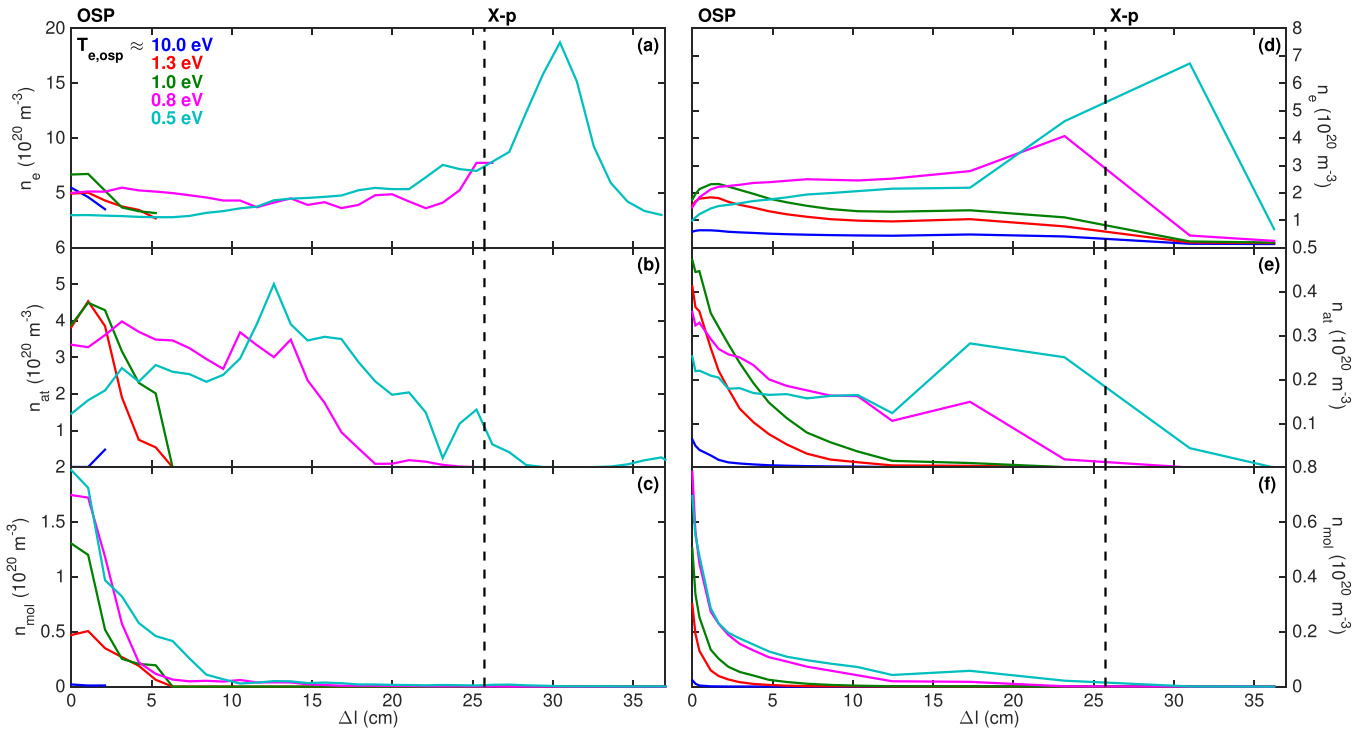


Figure 9. Experimental estimates (a)–(c) and EDGE2D-EIRENE predictions (d)–(f) of poloidal profiles of the electron (a), (d), atomic (b), (e) and molecular (c), (f) densities at $T_{e,osp} \approx 10.0$ eV (blue), $T_{e,osp} \approx 1.3$ eV (red), $T_{e,osp} \approx 1.0$ eV (green), $T_{e,osp} \approx 0.8$ eV (magenta) and $T_{e,osp} \approx 0.5$ eV (cyan). The Δl coordinate measures the distance from the outer strike point ($\Delta l = 0$) along the path illustrated in figure 4. The vertical black dashed line marks the location of the X-point along the path.

found to first increase near the strike point and extend upstream with decreasing $T_{e,osp}$, while remaining primarily below the X-point. A detailed discussion on the evolution of the n_e and n_{at} distributions during the detachment process can be found in [20], while the effect of considering the molecularly induced emission on the estimate of n_{at} is investigated in section 5.3.

Unlike n_e and n_{at} , figures 8(g)–(i) and 9(c) and f show the molecular density distribution consistently peaking at the outer strike point and extending only 5–10 cm upstream at all divertor temperatures. Here, the presented n_{mol} is inferred from the D_α emission, while the D_γ emission provides approximately similar estimates with significantly higher uncertainties due to the lower molecularly induced emission contributions, as demonstrated in section 5.2. The molecular density is observed to increase monotonously with decreasing $T_{e,osp}$, locally reaching values comparable to the upstream-shifted electron density both in the experimental analysis and the EDGE2D-EIRENE predictions in figures 9(c) and f, respectively.

Comparison between figures 5 and 9 reveals significantly closer qualitative resemblance between the spatial characteristics of the divertor n_{mol} and the molecularly induced Balmer D_α emission component than between n_{mol} and either the experimentally recorded emission around 602.0 nm or the Fulcher- α emission calculated from EDGE2D-EIRENE output. The similarity is expected in the experimental analysis in which n_{mol} is inferred from the Balmer emission component

alone but is supported also by the EGDE2D-EIRENE predictions for which both of the studied emission contributions are calculated based on n_{mol} . This indicates that distinguishing the molecularly induced Balmer emission from the purely atomic Balmer emission provides improved capabilities for observing molecules in the divertor plasma in comparison to the established spectroscopic measurements of the Fulcher band emission, even if the Fulcher- α emission was successfully distinguished from the bremsstrahlung contribution.

5.2. Evolution of n_{mol} at outer strike point during detachment

As suggested by the poloidal profiles in figures 9(c) and 10(a) shows the molecular density increasing at the outer strike point with decreasing $T_{e,osp}$. The molecules emerge at low temperatures of $T_{e,osp} < 2.0$ eV with more noticeable increase at $T_{e,osp} < 1.0$ eV below the roll-over temperature of the target ion current. At the lowest temperatures, n_{mol} increases by a factor of 3–5 between $T_{e,osp} = 0.7$ eV and $T_{e,osp} = 0.5$ eV, but the data is affected by large uncertainties due to the sensitivity of the production rate of the H_2^+ ions to changes in T_e in this range, as visualized in figure 2(f). The ratio between the molecular and electron densities at the outer strike point in figure 10(b) suggests n_{mol} reaching 30%–50% of the magnitude of n_e , as the strike point temperature decreases to $T_{e,osp} \approx 0.7$ eV, and increasing steeply to equal it at $T_{e,osp} <$

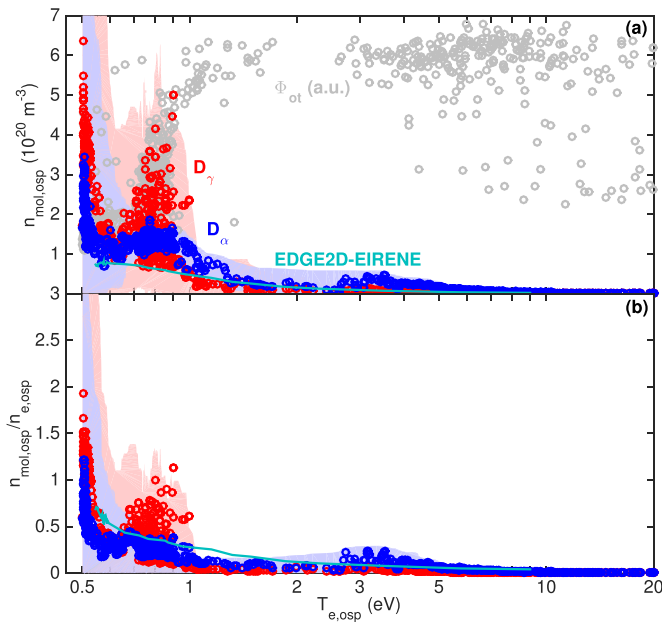


Figure 10. Molecular density (a) and its ratio to the electron density (b) at the outer strike point inferred experimentally from the molecularly induced D_α (blue) and D_γ (red) emission with comparison to EDGE2D-EIRENE predictions (cyan) as functions of the outer strike point electron temperature. The shaded areas represent the error estimates of the experimentally inferred n_{mol} . The outer target ion current (grey) is presented in (a) in arbitrary units as a guideline for the detachment process. Note the logarithmic x axes. Adapted from [41]. © IOP Publishing Ltd. All rights reserved.

0.6 eV. As noted above, however, the uncertainties of the analysis are large at the lowest temperatures.

The molecular densities inferred separately from D_α and D_γ emissions agree within their uncertainties in figure 10(a), albeit the D_γ data shows significantly wider scatter and larger uncertainties at $T_{e,\text{osp}} = 0.7\text{--}1.0$ eV. This is due to the decreased accuracy of the optimization of the molecularly induced emission fraction and the consequently larger relative uncertainties of the data for low emission contributions typical to D_γ , as demonstrated in [41]. The reasonable agreement between the n_{mol} estimates, inferred from the independent and unconstrained estimates for the molecularly induced D_α and D_γ emission fractions is, nevertheless, a supportive sign of the performance of the optimization model in successfully finding solutions for the latter.

The EDGE2D-EIRENE simulations predict molecular densities within the uncertainties of the experimental analysis at the outer strike point in figure 10(a), albeit the simulations following the low end of the experimental data at $T_{e,\text{osp}} < 1.0$ eV, remaining approximately a factor of 2 below the bulk of the data points. However, also the simulated electron density was found to remain a factor of 2–4 below the experimental estimate at the outer strike point in [20], rendering direct quantitative comparison of the densities infeasible between the experiments and the simulations. When this difference is primitively considered by investigating the $\frac{n_{\text{mol,osp}}}{n_{e,\text{osp}}}$ ratio in figure 10(b), the agreement within experimental uncertainties

remains, but the EDGE2D-EIRENE predictions suggest on average slightly higher molecular densities with respect to the local electron density.

5.3. Effect of molecularly induced emission on estimate of atomic density

In [20], it was postulated that the molecularly induced emission, previously unaccounted for, led to overestimation of the atomic density. Due to n_e and T_e being constrained by the line-integrated spectroscopic measurements in the optimization process, the molecularly induced emission was considered to be likely misinterpreted as an increase in the electron-impact excitation component via an increase in n_{at} for which similar constraints do not exist. The hypothesis was tested by comparing the n_{at} solutions of the amended model presented here to the estimates given by the original model in [20], as well as by performing the optimization with and without the inclusion of the $f_{\text{mol},\alpha}$ and $f_{\text{mol},\gamma}$ variables using synthetic emission calculated from the EDGE2D-EIRENE simulation outputs, including the molecularly induced emission contribution in both cases.

As expected, a decrease by up to a factor of 2 is observed in the experimental n_{at} estimate at the outer strike point in figure 11(a), when the molecularly induced emission is considered in the optimization model. The effect is the strongest at $T_{e,\text{osp}} = 0.9\text{--}1.2$ eV on both sides of the roll-over of the target ion current, when the molecularly induced emission is at its strongest, but at $T_{e,\text{osp}} < 0.9$ eV, no difference is observed between the estimates with and without the inclusion of the $f_{\text{mol},\alpha}$ and $f_{\text{mol},\gamma}$ variables. This is partly attributed to the decrease in the molecularly induced emission in figure 6, but is most likely due to the contribution of the electron-impact excitation component—the only emission component with an n_{at} dependence in equation (1)—decreasing to insignificantly low levels with decreasing $T_{e,\text{osp}}$ in figure 11(b). The reliability of the n_{at} estimate in detached conditions is thus uncertain.

Similar examination with synthetic emission from EDGE2D-EIRENE simulations in figures 11(c) and d shows an approximately identical effect as in the experimental analysis with a corresponding factor-of-2 decrease in the n_{at} estimate near the roll-over of Φ_{ot} and agreement of the estimates between the original and amended models at the lowest temperatures. Despite the observed decrease in the n_{at} estimate, a comparison to the true outer strike point n_{at} taken directly from the EDGE2D-EIRENE output in figure 11(c) indicates overestimation of the local n_{at} by up to a factor of 3 in the optimization model. While the n_{at} estimated from the synthetic emission is found to agree within its uncertainties with the reference at $T_{e,\text{osp}} > 1.4$ eV, when the relative contribution of the excitation component exceeds 5% in figure 11(d), the remaining overestimation at low temperatures underlines the significant challenges in extracting information on atomic densities at detachment-relevant low temperatures with the emission dominated by recombination.

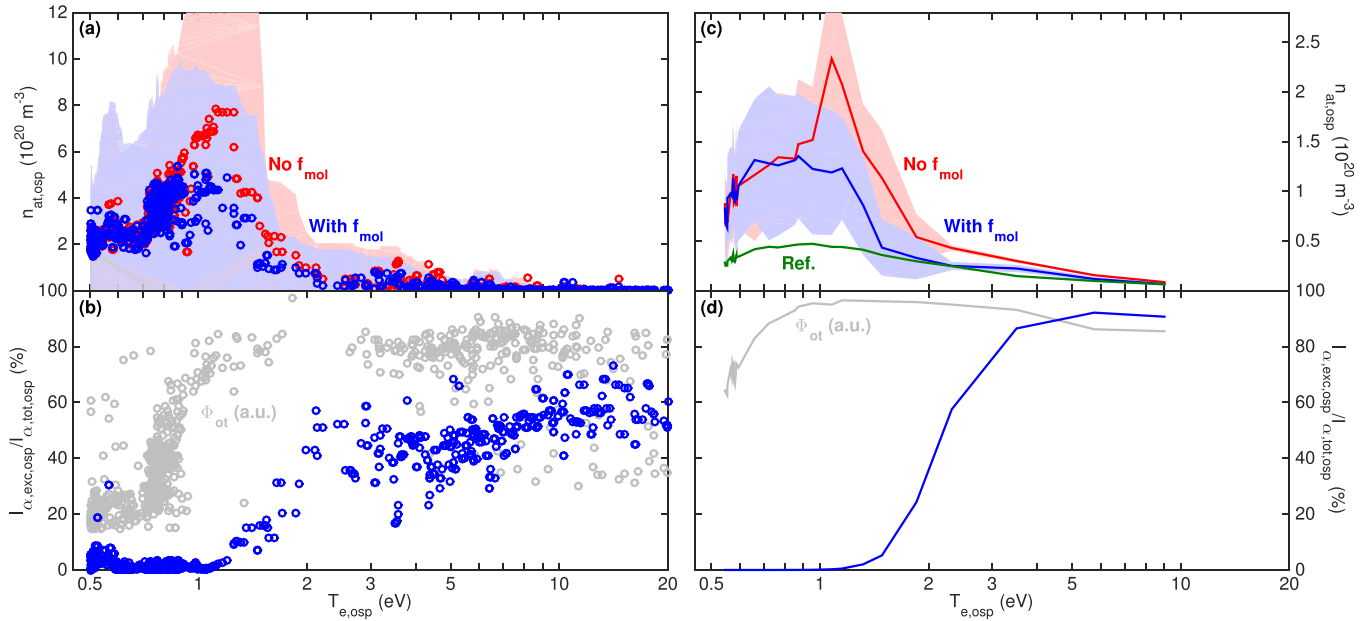


Figure 11. Estimates of the atomic density (a), (c) obtained with optimization models with (blue) and without (red) the inclusion of the $f_{\text{mol},\alpha}$ and $f_{\text{mol},\gamma}$ variables together with the fraction of the electron-impact excitation component in the total D_α emission intensity (b), (d) at the outer strike point as functions of the strike point electron temperature in the experimental analysis (a), (b) and the EDGE2D-EIRENE simulations (c), (d). The shaded areas in (a), (c) represent the error estimates of the experimentally inferred n_{at} , and the green curve in (c) provides true local $n_{\text{at},\text{osp}}$ reference directly from the EDGE2D-EIRENE output. The outer target ion current (grey) is presented in (b), (d) in arbitrary units as a guideline for the detachment process. Note the logarithmic x axes.

6. Conclusions

Experimental distinction of the deuterium Balmer line emission contribution arising from molecular processes was enabled by amending a previously presented optimization model for generating 2D estimates of divertor plasma conditions from tomographic reconstructions of divertor camera images. The molecularly induced emission was further used for inferring the molecular divertor density within the Balmer emission regions, utilizing the AMJUEL and H2VIBR atomic and molecular databases. The method was applied experimentally in a JET L-mode density scan with the outer divertor ranging from high-recycling conditions to deep detachment, while indicative qualitative reference and detailed investigation of the different emission components was provided by a set of EDGE2D-EIRENE simulations which covered the experimentally observed divertor T_e range, albeit not achieving as high divertor n_e and deep detachment as in the experiment.

The molecular processes were found to account for up to 60%–70% of the D_α emission and 10%–20% of the D_γ emission in the vicinity of the outer strike point at the onset of detachment, while increased dominance of the electron-ion recombination component was observed with deepening detachment. The experimental estimates of the molecularly induced emission fractions agreed primarily within uncertainties with predictions calculated from the EDGE2D-EIRENE simulation output with the available molecular reaction rates for hydrogen, indicating physically valid performance of the method and reasonable approximation provided by the hydrogen rates for describing molecular processes in deuterium

plasmas. The comparison between the experimental analysis and the modelling was also found to support the assumed absence of negative D^- ions in deuterium plasmas despite their predicted prominent role in hydrogen plasmas.

The derived estimates for the molecularly induced D_α and D_γ emission contributions were found to agree on the dominance of the molecular processes at the onset of detachment with recent studies at TCv [35, 36], while providing insight also on the development of the role of molecular processes at deeper states of detachment. The maximum molecularly induced emission contributions were 20%–30% lower at JET than those observed at TCv, which was attributed to increased fraction of reflected atoms in the recycling flux from the tungsten divertor of JET in comparison to the carbon divertor of TCv, as well as an expectation of stronger role of electron-ion recombination at the higher divertor densities of JET.

The molecular divertor density, inferred from the molecularly induced Balmer emission components, was observed to increase to the level of $n_{\text{mol},\text{osp}} = 1\text{--}2 \times 10^{20} \text{ m}^{-3}$, when the outer strike point temperature decreased from $T_{e,\text{osp}} \approx 2.0 \text{ eV}$ to $T_{e,\text{osp}} \approx 0.7 \text{ eV}$, corresponding to approximately 30%–50% of the local electron density. At the lowest end of the studied temperature range, $n_{\text{mol},\text{osp}}$ was found to increase rapidly to equal $n_{e,\text{osp}}$, albeit with the estimate being characterized by significant uncertainties due to sensitivity of the molecular reaction rates to small changes in low T_e . Agreement within the uncertainties was observed between the molecular densities inferred from the independent solutions of estimates for the molecularly induced D_α and D_γ fractions. While a direct comparison between the experimental analysis and the EDGE2D-EIRENE predictions was not feasible due to

noticeable differences in the divertor n_e , the two analyses were found to agree on the $\frac{n_{\text{mol}}}{n_e}$ ratio at the outer strike point within the uncertainties of the experimental data. In addition to enabling the inference of n_{mol} , the consideration of the molecularly induced emission was also found to improve the estimate of the atomic density at the onset of detachment.

The agreement between the amended experimental analysis method and modelling predictions on the evolutions of the molecularly induced Balmer D_α and D_γ emission components and the molecular density estimates inferred from them indicate prospects for broader range of applications of the 2D camera measurements of Balmer line emission in diagnosing the divertor plasma conditions experimentally. While the emission fractions are allowed to range freely in the optimization process with no ties to physical models, the inference of the molecular density is, however, prone to the assumptions made on, e.g. the vibrational excitation of the molecules, as well as the potential isotope effects between the available molecular reaction rates for hydrogen and the studied deuterium plasmas. Deeper understanding of the molecular physics with the different isotopes of hydrogen is thus needed for further validation of the method and, consequently, more accurate interpretation of the divertor emission.

Data availability statement

The data that support the findings of this study are available upon reasonable request from the authors.

Acknowledgments

This work has been carried out within the framework of the EUROfusion Consortium and has received funding from the Euratom research and training programme 2014–2018 and 2019–2020 under Agreement No. 633053. The views and opinions expressed herein do not necessarily reflect those of the European Commission.

ORCID iDs

J Karhunen  <https://orcid.org/0000-0001-5443-518X>
 A Holm  <https://orcid.org/0000-0002-8391-8364>
 V Solokha  <https://orcid.org/0000-0002-1738-1757>
 M Groth  <https://orcid.org/0000-0001-7397-1586>
 K D Lawson  <https://orcid.org/0000-0002-1251-6392>

References

- [1] Itami K, Coad P, Fundamenski W, Ingesson C, Lingertat J, Matthews G F and Tabasso A 2001 *J. Nucl. Mater.* **290–293** 633–8
- [2] Huber A et al 2003 *J. Nucl. Mater.* **313–316** 925–30
- [3] Huber A et al 2012 *Rev. Sci. Instrum.* **83** 10D511
- [4] Harrison J, Lisgo S W, Gibson K J, Tamain P, Dowling J and MAST Team T 2011 *J. Nucl. Mater.* **415** S379–82
- [5] Huber A et al 2013 *J. Nucl. Mater.* **438** S139–47
- [6] Karhunen J et al 2019 *Rev. Sci. Instrum.* **90** 103504
- [7] Fenstermacher M E, Meyer W H, Wood R D, Nilson D G, Ellis R and Brooks N H 1997 *Rev. Sci. Instrum.* **68** 974
- [8] Fenstermacher M E et al 1997 *J. Nucl. Mater.* **241–243** 666–71
- [9] Leonard A W et al 1999 *J. Nucl. Mater.* **266–269** 348–53
- [10] Boswell C J, Terry J L, Lipschultz B and Stillerman J 2001 *Rev. Sci. Instrum.* **72** 935
- [11] Duval B P et al 1999 *Bull. Am. Phys. Soc.* **44** G175
- [12] Harrison J et al 2017 *Nucl. Mater. Energy* **12** 1071–6
- [13] Perek A et al 2019 *Rev. Sci. Instrum.* **90** 123514
- [14] Perek A et al 2021 *Nucl. Mater. Energy* **26** 100858
- [15] Harhausen J, Kallenbach A and Fuchs C 2011 *Plasma Phys. Control. Fusion* **53** 025002
- [16] Odstřčil M et al 2014 *Rev. Sci. Instrum.* **85** 013509
- [17] Agostini M, Vianello N, Carraro L, Carralero D, Cavedon M, Dux R, Naulin V, Spolaore M and Wolfrum E 2019 *Plasma Phys. Control. Fusion* **61** 115001
- [18] Bowman C, Harrison J R, Lipschultz B, Orchard S, Gibson K J, Carr M, Verhaegh K and Myatra O 2020 *Plasma Phys. Control. Fusion* **62** 045014
- [19] Karhunen J, Lomanowski B, Solokha V, Aleiferis S, Carvalho P, Groth M, Kumpulainen H, Lawson K D, Meigs A G, Shaw A 2020 *Nucl. Mater. Energy* **25** 100831
- [20] Karhunen J, Lomanowski B, Solokha V, Aleiferis S, Carvalho P, Groth M, Lawson K D, Meigs A G and Shaw A 2021 *Plasma Phys. Control. Fusion* **63** 085018
- [21] Perek A et al 2021 *Nucl. Fusion* submitted
- [22] Lumma D, Terry J L and Lipschultz B 1997 *Phys. Plasmas* **4** 2555
- [23] Lomanowski B, Groth M, Coffey I, Karhunen J, Maggi C F, Meigs A G, Menmuir S and O'Mullane M 2020 *Plasma Phys. Control. Fusion* **62** 065006
- [24] Meigs A G et al 2000 *27th EPS Conf. on Plasma Physics* pp 1264–7
- [25] Potzel S, Dux R, Müller H W, Scarabosio A and Wischmeier M 2014 *Plasma Phys. Control. Fusion* **56** 025010
- [26] Lomanowski B, Meigs A G, Sharples R M, Stamp M and Guillemaut C 2015 *Nucl. Fusion* **55** 123028
- [27] Verhaegh K et al 2019 *Nucl. Fusion* **59** 126038
- [28] Nishizawa T, Cavedon M, Reimold F, Dux R, Brida D and Wu H 2020 *Plasma Phys. Control. Fusion* **62** 085005
- [29] Lomanowski B et al 2019 *Nucl. Mater. Energy* **20** 100676
- [30] Bates D R, Kingston A E and McWhirter R W P 1962 *Proc. R. Soc. A* **267** 297
- [31] Summers H P and McWhirter R W P 1979 *J. Phys. B: At. Mol. Phys.* **12** 2387
- [32] Summers H P, Dickson W J, O'Mullane M G, Badnell N R, Whiteford A D, Brooks D H, Lang J, Loch S D and Griffin D C 2006 *Plasma Phys. Control. Fusion* **48** 263–93
- [33] Wunderlich D and Fantz U 2016 *Atoms* **4** 26
- [34] Reiter D et al 2018 *23rd Int. Conf. on Plasma Surface Interactions in Controlled Fusion Devices*
- [35] Verhaegh K et al 2021 *Plasma Phys. Control. Fusion* **63** 035018
- [36] Verhaegh K et al 2021 *Nucl. Mater. Energy* **26** 100922
- [37] Menmuir S, Rachlew E, Fantz U, Pugno R and Dux R 2007 *J. Quant. Spectrosc. Radiat. Transfer* **105** 425–37
- [38] Lomanowski B et al 2018 *23rd Int. Conf. on Plasma Surface Interactions in Controlled Fusion Devices*
- [39] Groth M et al 2019 *Nucl. Mater. Energy* **19** 211–7
- [40] Dey R et al 2019 *Nucl. Fusion* **59** 076005
- [41] Karhunen J, Holm A, Lomanowski B, Solokha V, Aleiferis S, Carvalho P, Groth M, Lawson K D, Meigs A G, Shaw A 2022 *J. Instrum.* **17** C01032
- [42] Simonini R, Corrigan G, Radford G, Spence J and Taroni A 1994 *Contrib. Plasma Phys.* **34** 368
- [43] Reiter D et al 1992 *J. Nucl. Mater.* **196–198** 80–89
- [44] Wiesen S 2006 EDGE2D/EIRENE code interface report *JET ITC-Report* (available at: www.eirene.de/e2deir_report_40jun06.pdf)
- [45] Summers H P 2004 *The ADAS User Manual, version 2.6* (available at: www.adas.ac.uk)

- [46] Hastings W K *et al* 1970 *Biometrika* **57** 97–109
- [47] Patil A Huard D and Fannesbeck C 2010 *J. Stat. Softw.* **35** 1–81
- [48] Kotov V , Reiter D, Kukushkin A S, Pacher H D, Börner P and Wiesen S 2006 *Contrib. Plasma Phys.* **46** 635–42
- [49] Kotov V *et al* 2006 *33rd EPS Conf. on Plasma Physics* P–1.128
- [50] Kotov V *et al* 2007 Numerical study of the ITER divertor plasma with the B2-EIRENE code package *Juel-4257*
- [51] Behringer K and Fantz U 2000 *New J. Phys.* **2** 23
- [52] Reiter D 2020 The data file AMJUEL: additional atomic and molecular data for EIRENE (available at: www.eirene.de/amjuel.pdf)
- [53] Reiter D 2017 The data file H2VIBR: additional atomic and molecular data for EIRENE (available at: www.eirene.de/h2vibr.pdf)
- [54] Holm A , Börner P, Rognlien T D, Meyer W H and Groth M 2021 *Nucl. Mater. Energy* **27** 100982
- [55] Wunderlich D, Dietrich fnmS and Fantza U 2009 *J. Quant. Spectrosc. Radiat. Transfer* **110** 62–71
- [56] Wunderlich D *et al* 2020 *J. Quant. Spectrosc. Radiat. Transfer* **240** 106695
- [57] Holm A, Wunderlich D, Groth M and Börner P 2022 *Contrib. Plasma Phys.* **e202100189**
- [58] Bardsley J N and Wadehra J M 1979 *Phys. Rev. A* **20** 1398–405
- [59] Krishnakumar E *et al* 2011 *Phys. Rev. Lett.* **106** 243201
- [60] Rapp D *et al* 1965 *Phys. Rev. Lett.* **14** 533
- [61] Fantz U *et al* 2001 *J. Nucl. Mater.* **290–293** 367–73
- [62] Fantz U *et al* 2001 *Plasma Phys. Control. Fusion* **43** 907–18
- [63] Xiao B *et al* 2004 *Plasma Phys. Control. Fusion* **46** 653–68
- [64] Hollmann E M *et al* 2006 *Plasma Phys. Control. Fusion* **48** 1165–80
- [65] Sergienko G *et al* 2013 *J. Nucl. Mater.* **438** S1100–3
- [66] Terakado A *et al* 2019 *Nucl. Mater. Energy* **20** 100679
- [67] Saito S *et al* 2020 *Contrib. Plasma Phys.* **60** e201900152
- [68] Järvinen A *et al* 2013 *40th EPS Conf. on Plasma Physics* P2.130
- [69] Järvinen A *et al* 2016 *Nucl. Fusion* **56** 046012